Journal of Alloys and Compounds 1080 (2026) 190423

Contents lists available at ScienceDirect

Journal of Alloys and Compounds

journal homepage: www.elsevier.com/locate/jalcom

Formation and mechanical properties of oriented lamellar microstructures in a β-solidifying γ-TiAl alloy fabricated by laser powder bed fusion

Sung-Hyun Park [a], Ozkan Gokcekaya [a,b], Kazuhisa Sato [c], Hyoung Seop Kim [d], Myung-Hoon Oh [e], Takayoshi Nakano [a,b,*]

[a] Division of Materials and Manufacturing Science, Graduate School of Engineering, The University of Osaka, 2-1, Yamadaoka, Suita, Osaka 565-0871, Japan
[b] 3DPTec Integrated Center, Graduate School of Engineering, The University of Osaka, 2-1, Yamadaoka, Suita, Osaka 565-0871, Japan
[c] Research Center for Ultra-High Voltage Electron Microscopy, The University of Osaka, 7-1 Mihogaoka, Ibaraki, Osaka 567-0047, Japan
[d] Graduate Institute of Ferrous & Eco Materials Technology, Pohang University of Science and Technology (POSTECH), Pohang 37673, South Korea
[e] School of Materials Science and Engineering, Kumoh National Institute of Technology (KIT), 61 Daehakro, Gumi, Gyeongbuk 39177, Republic of Korea

ARTICLE INFO

Keywords:
Laser powder bed fusion, γ-TiAl alloy,
Crystallographic texture
Variant selection
Oriented lamellae

ABSTRACT

A highly oriented lamellar microstructure was achieved in a β-solidifying γ-titanium aluminide (γ-TiAl) alloy fabricated via laser powder bed fusion (L-PBF) followed by heat treatment. The investigated alloy composition was Ti-44Al-6Nb-1.2Cr (at%), the optimized processing condition resulted in β_o/α_2 lamellae aligned parallel to the build direction (BD) and α_2/6H long-period stacking ordered (LPSO) lamellae tilted at ± 45° from the BD. The β_o/α_2 lamellae were completed by the formation of a single crystalline-like texture with {011}z <100>x orientation in β phase, variant selection in α_2 phase with the Burgers orientation relationship. Additionally, the 6H-LPSO structure, which formed from the α_2 phase, was aligned parallel to the $(0001)\alpha_2$ plane after heat treatment. Thus, the orientation of α_2/6H-LPSO was determined by the previous as-built crystallographic texture and subsequent variant selection in the α_2 phase.

The heat-treated specimen exhibited superior mechanical properties, achieving a tensile strength to fracture of 475.2 ± 52.1 MPa at room temperature and a yield strength of 523.7 ± 8.5 MPa, an ultimate tensile strength of 705.5 ± 21.4 MPa, and an elongation of 8.5 ± 1.4% at 800 °C, respectively. The enhanced strength was mainly attributed to the refined microstructure induced by the rapid solidification characteristics of the L-PBF process, which effectively impeded dislocation motion. In addition, the highly oriented lamellar microstructure promoted tortuous crack propagation accompanied by crack deflection and branching, thereby enhancing damage tolerance and elongation. Consequently, the present study demonstrates the strong potential of the L-PBF process for advanced microstructural control in high-performance γ-TiAl alloys.

1. Introduction

γ-Titanium aluminide (γ-TiAl) alloys are attractive structural materials for aerospace and automotive industries due to their low density, good strength retention at high temperatures, and excellent creep resistance [1,2]. Over the past few decades, extensive research has been conducted to establish the materials–process–manufacturing foundations of γ-TiAl alloys, and some of these developments have been successfully implemented, such as low-pressure turbine blades for aero-engines and turbocharger wheels in automotive engines [3–6]. However, several challenges have hindered the broader practical application of γ-TiAl alloys. For instance, the conventional investment casting process, widely used for γ-TiAl alloys, suffers from high reactivity with oxygen and nitrogen during processing [7,8]. This often results in the formation of a reaction layer at the mold–metal interface, degrading surface quality and promoting crack propagation. Moreover, post-processing steps such as grinding and machining are inefficient and costly.

Given the ongoing issues associated with traditional methods, alternative manufacturing approaches such as additive manufacturing (AM) have become increasingly attractive. In fact, the fabrication of γ-TiAl alloy components using the electron beam powder bed fusion (EB-

* Corresponding author at: Division of Materials and Manufacturing Science, Graduate School of Engineering, The University of Osaka, 2-1 Yamadaoka, Suita, Osaka 565-0871, Japan.
E-mail address: nakano@mat.eng.osaka-u.ac.jp (T. Nakano).

https://doi.org/10.1016/j.jallcom.2026.190423
Received 11 June 2026; Received in revised form 31 July 2026; Accepted 12 August 2026
Available online 12 August 2026

PBF) process has been extensively explored [9–11], and the process has proven to be a promising approach. The vacuum environment of the EB-PBF is particularly advantageous for minimizing oxidation during the fabrication. In addition, the high build temperature helps to relieve residual stresses and prevent cracking, which is especially beneficial when processing inherently brittle materials, including γ-TiAl alloys. On the other hand, the successful fabrication of γ-TiAl alloys using the laser powder bed fusion (L-PBF) process remains limited. The majority of existing research has focused primarily on mitigating cracking due to the inherent brittleness [12–14]. Moreover, studies aimed at enhancing mechanical properties through the combination of a comprehensive understanding and control of microstructure are still underexplored.

In recent years, it has become evident that the L-PBF process offers unique capabilities in controlling crystallographic texture. For instance, a single-crystalline-like texture with <001>, <011> , and <111> orientations along the building direction (BD) has been demonstrated in β-Ti alloys [15,16]. Additionally, crystallographic lamellar microstructures with a dominant <110> orientation and a minor <100> orientation component have been reported in 316 L stainless steel and Inconel 718 alloys [17,18]. These results highlight the crystallographic texture feasibility in cubic alloy systems, and the unique features of the L-PBF process present new opportunities for enhancing material performance through anisotropic characteristics [19,20]. Meanwhile, γ-TiAl alloys are also known to exhibit strong anisotropic mechanical behavior, which arises from the angle between the lamellar orientation and the loading direction [21,22]. The resulting aligned lamellar microstructure has been reported to enhance strength, toughness, and fatigue resistance at both room and elevated temperatures [23–26], suggesting that controlling the lamellar orientation in γ-TiAl alloys is critical for optimizing their mechanical performance.

Such lamellar orientation in γ-TiAl alloys is determined by the crystallographic texture of the primary phase, and specific orientation relationship between the phases during the subsequent phase transformation, namely Burgers orientation relationship (OR) where $\{110\}_\beta$ // $(0001)_{\alpha2}$ and $<111>_\beta$ // $<11\bar{2}0>_{\alpha2}$ and Blackburn OR where $(0001)_{\alpha2}$ // $\{111\}_\gamma$ and $<11\bar{2}0>_{\alpha2}$ // $<1\bar{1}0>_\gamma$, respectively [27,28]. Therefore, we attempted to utilize the L-PBF process with β-solidifying γ-TiAl alloys to achieve an oriented lamellar microstructure for enhanced mechanical properties. To this end, this study investigated the development of β_o phase crystallographic texture, subsequent α_2 variant selection during the phase transformation, and the evolution of lamellar characteristics during post-process heat treatment in a highly dense Ti−44Al−6Nb−1.2Cr (at%) alloy fabricated by the L-PBF process.

2. Materials and methods

2.1. Sample preparation

Gas-atomized Ti−44Al−6Nb−1.2Cr alloy powder (Osaka Titanium Technologies, Japan) with a spherical morphology and a mean diameter of 36.0 μm was used as the starting material. The nominal composition of powder was Ti (balance), Al (43.77 at%), Nb (5.96 at%), and Cr (1.22 at%) as determined by inductively coupled plasma optical emission spectroscopy. More detailed information on powder characteristics can be found in previous studies [29,30]. As depicted in Fig. 1a, the L-PBF (EOS M290, EOS, Germany) machine was used to fabricate two types of cuboid specimens with dimensions of 5 × 5 × 5 mm for microstructural characterization and 5 × 5 × 20 mm for evaluation of mechanical properties. The fabrication was carried out in an Ar atmosphere, with a baseplate temperature of 200 ℃ to mitigate thermal stress. A bidirectional scanning strategy along the scanning direction was applied without a rotation between layers.

To investigate the effect of process parameters on densification behavior, 5 × 5 × 5 mm cubic specimens were fabricated under various processing conditions. A constant laser power (P) of 180 W and a layer thickness (h) of 60 μm, while the scanning speed (v) and hatch spacing (d) were varied in the ranges of 600–1000 mm/s and 10–60 μm, respectively. The volumetric energy density (VED) for these processing conditions was calculated to range from 50 to 500 J/mm^3 according to Eq. (1):

$$\mathrm{VED} = \frac{P}{v \bullet d \bullet t} \tag{1}$$

Based on the results of the parameter exploration shown in Fig. 1b, a volumetric energy density (VED) of 375 J/mm^3 was selected as the optimal processing condition for further investigation. The specific process parameters for the optimized condition were a laser power (P) of 180 W, a scanning speed (v) of 800 mm/s, a hatch spacing (d) of 10 μm, and a layer thickness (h) of 60 μm, resulting in almost full densification (relative density of 99.97%) with negligible porosity and no observable cracks, consistent with the densification behavior reported in our previous studies [31,32]. This enhanced densification behavior was attributed to thermal accumulation from adjacent scan tracks, which reduced the cooling rate and relieved residual stress, and partial

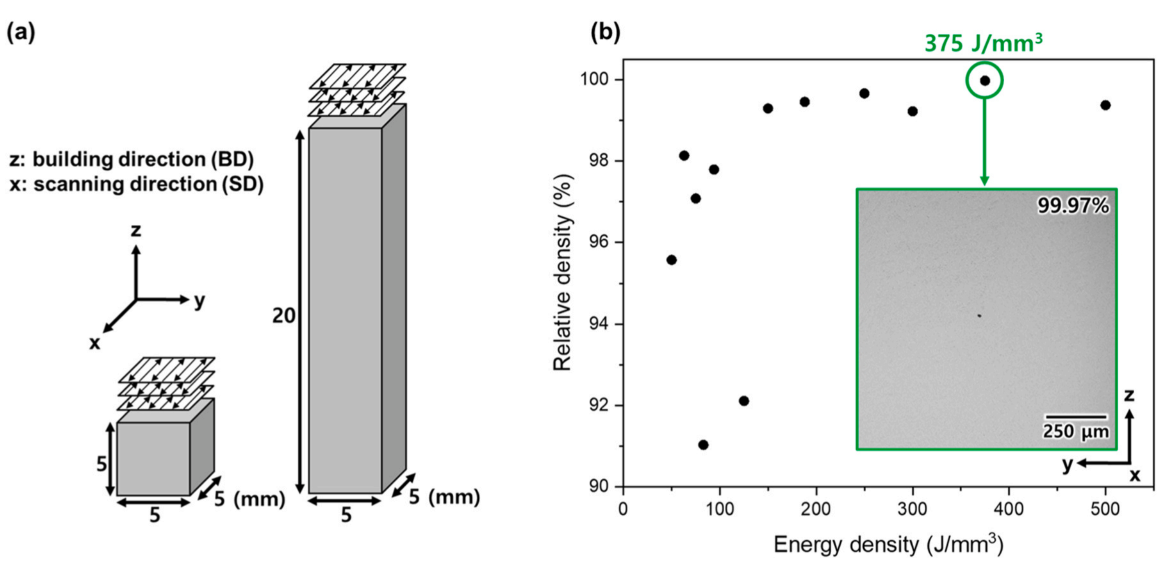

Fig. 1. (a) Schematic illustrations of short and long cuboid samples fabricated by the L-PBF process with the scanning strategy and (b) a plot of relative density–VED, with an inset showing a representative optical microscopy image of the y–z cross-sections under the optimized process condition.

remelting behavior, which refilled pre-existing pores and cracks.

2.2. Microstructure characterization of as-built and heat-treated samples

The microstructural characteristics of the as-built and heat-treated specimens were examined using field-emission scanning electron microscopy (FE-SEM; JIB-4610F, JEOL, Japan) equipped with an electron backscatter diffraction (EBSD; NordlysMax[3], Oxford Instruments, UK) system. Cuboid samples with dimensions of 5 × 5 × 5 mm were used for the microstructural analyses. Prior to observation, all specimens were mechanically polished using emery paper, followed by final chemical polishing with colloidal silica to obtain mirror-finished surfaces.

In addition, heat treatment of the as-built specimens was carried out at 850 ℃ for 6 h followed by furnace cooling, aiming to form lamellar colonies. This heat treatment is comparable to the second step of the conventional two-step heat treatment typically applied to γ-TiAl alloys, known as stabilization or precipitation treatment [33]. For the detailed observation of the lamellar characteristics, a transmission electron microscope (TEM; JEM-ARM200F, JEOL, Japan) was used.

2.3. Mechanical testing

Only heat-treated specimens were subjected to tensile testing at room and high temperatures to evaluate the mechanical properties under a stabilized microstructure, since the as-built condition may cause unexpected microstructural changes during high-temperature testing. Sub-sized tensile specimens with gauge dimensions of 5.0 × 1.5 × 0.5 mm were sectioned from the 5 × 5 × 20 mm cuboid samples and heat-treated under the same conditions described above. In addition, the testing specimens were also polished using emery papers and colloidal silica to minimize the influence of surface roughness during the mechanical tests. Tensile properties were evaluated using a universal testing machine (AG-5000C, Shimadzu, Japan) at room temperature and 800℃ under vacuum conditions, with a strain rate of $1.7 \times 10^{-4}\ s^{-1}$. After the tensile tests, thin foils were extracted from regions near the fracture surface for TEM observation of the deformation microstructure, while the fracture surfaces were examined using FE-SEM to investigate the crack propagation behavior.

3. Results and discussion

3.1. Microstructure of as-built specimen under optimized processing conditions

Fig. 2 shows the microstructures of the as-built Ti−44Al−6Nb−1.2Cr alloy specimen fabricated via the L-PBF process, observed on two different planes. From the SEM-backscattered electron (SEM-BSE) images, the β_o, α_2, and γ phases appear as white, gray, and black contrasts, respectively. Such contrast is commonly observed in TiAl-based alloys, where these phases can be clearly distinguished by their characteristic brightness. Therefore, the microstructure was mainly composed of precipitated α_2 phase within β_o matrix, along with a small amount of γ phase distributed in the β_o phase (Figs. 2a and 2b). However, these microstructural features differ from the α_2/γ lamellae typically observed in conventionally processed γ-TiAl alloys [34,35]. In general, during conventional processes such as casting, the solid-state β → α transformation can result in the nucleation of multiple α grains with different orientations within a single β grain, leading to β-segregations along the interfaces between the β and α grains. Upon subsequent cooling, the α_2/γ lamellar microstructure develops from the parent α phase according to the Blackburn OR [35]. In contrast, the rapid cooling characteristics of the L-PBF process suppressed complete phase transformation, resulting in the absence of α_2/γ lamellar microstructure [12,36,37]. In addition, it is an interesting note that the morphology of β_o and α_2 phases varied depending on the observation planes. In the x-y plane (Fig. 2a), the precipitated α_2 phase appeared with diagonal and horizontal orientations. Whereas, it was predominantly aligned parallel to the BD, with a minor fraction showing horizontal orientation in the y-z plane (Fig. 2b).

For more detailed microstructural analysis, SEM-EBSD was performed focusing on the β_o and α_2 phases, which are the dominant constituents of the as-built specimen, while the γ phase was not analyzed due to its minor fraction. As indicated with inverse pole figures (IPFs) and pole figures (PFs) of the β_o phase (Figs. 3a–c and 3h–j), the evolved crystallographic texture exhibited strong <011> alignment along the BD. Furthermore, the crystallographic texture of the α_2 phase fulfilled the Burgers OR, which was demonstrated through coincident pole positions of between $\{110\}_{\beta o}$ and $\{0001\}_{\alpha 2}$ (Figs. 3e–g and l–n). In particular, three types of α_2 variants, which were inclined counterclockwise (pink), inclined clockwise (purple), and horizontally oriented (blue), formed triangular-shaped clusters in the x-y plane (Fig. 3d). The $\{0001\}_{\alpha 2}$ planes are inclined at ± 45° (pink and purple) and 0° (blue) with respect to the BD, corresponding to the three observed variants. Meanwhile, two types of α_2 variants (pink and pink salmon), whose $\{0001\}_{\alpha 2}$ planes are inclined at ± 45° with respect to the BD, were aligned along the BD, While a relatively small fraction of a third variant with horizontal orientation (green), whose $\{0001\}_{\alpha 2}$ planes is parallel to BD (0°), was observed in the y-z plane (Fig. 3k). This repeated formation of three types of α_2 variants indicates the occurrence of variant selection during β → α phase transformation.

Additionally, the crystallographic texture of the β_o phase and α_2 variants was examined across multiple grains within a wide region (Fig. 4). The observed IPF and PFs of the β_o phase consistently revealed that the $<110>_{\beta o}$ aligned to the BD, forming a single crystalline-like texture with slight misorientations between grains, and the α_2 phase followed the Burgers OR (Fig. 4a–e). From the $\{0001\}_{\alpha 2}$ PFs attributed to each β_o grain (Fig. 4f–h), it is clear that three α_2 variants were preferentially selected for each β_o grain, and the misorientation angle distributions of neighboring α_2 phases within primary β_o grains in the x-y

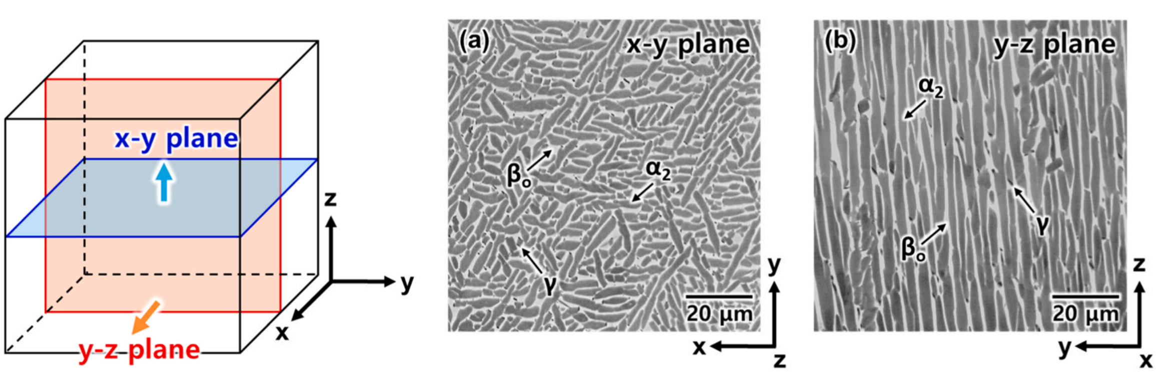

Fig. 2. Schematic representation showing the observation planes used for microstructural analysis, and SEM-BSE images of the as-built Ti−44Al−6Nb−1.2Cr alloy fabricated by the L-PBF process on the (b) x–y and (c) y–z planes, respectively.

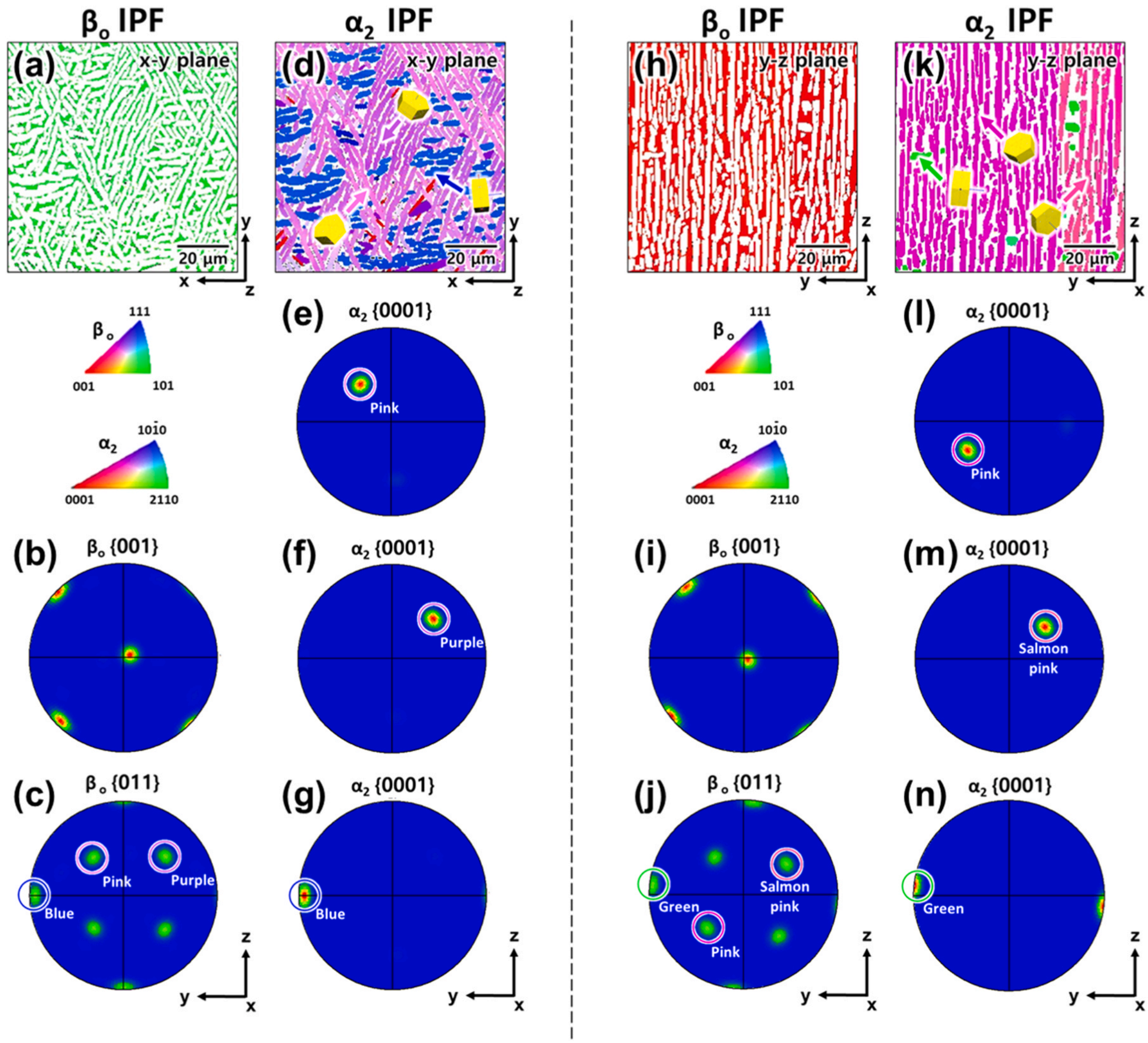

Fig. 3. IPF maps and PFs showing the crystallographic textures of the β_o and α_2 phases. (a–g) correspond to data obtained from the x–y plane: (a) β_o IPF map, (b, c) β_o PFs, (d) α_2 IPF map, (e–g) partial α_2 PFs. (h–n) represent data from the y–z plane: (h) β_o IPF map, (i, j) β_o PFs, (k) α_2 IPF map, (l–n) partial α_2 PFs.

plane exhibited a pronounced peak near 60° (Supplementary Fig. S1).

Theoretically, six variants of the $\{110\}_\beta$ plane correspond to twelve possible α variants that can be formed from a parent β phase according to the crystal symmetry. However, the formation of α variants does not occur randomly. This variant selection phenomenon is influenced by factors such as shape strain, interfacial energy, and crystallographic texture during the β → α phase transformation [38–40]. So that even various scan strategies affecting crystallographic texture development and resulting local lattice strains due to the complex thermal history of the AM process can notably influence the variant selection [41–43]. Among them, the previous calculations showed that strain was lowered through the combination of three α variants, and a high frequency of occurrence was observed when these clusters had misorientations of 60°/ $[11\bar{2}0]$ or 63.26°/ $[\bar{10}55\bar{3}]$ in quenched pure titanium [38]. Therefore, the preferential selection of three α_2 variants together with the pronounced misorientation peak near 60° suggests that the variant selection mechanism in this study is governed by the so-called self--accommodation, which minimizes the shape strain during the phase transformation.

However, on a larger scale, no distinct global α_2 variant selection was observed because each β_o grain randomly selected three variants locally. This random selection weakened the overall α_2 variant selection across the microstructure. A similar phenomenon can be found in the previous literature [44]. In addition, of the three α_2 variations, the specific one in which $\{0001\}_{\alpha 2}$ is parallel to BD (circled pole) is common. This is also true for another field of view, as shown in Fig. 3. Although the factors that contribute to this specific α_2 variant selection are not yet clear, the successful growth of this variant might require continuous solidification at a very low cooling rate. In the directional solidification process, a very low withdrawal rate has been used to form a 0°-oriented microstructure in γ-TiAl alloys [45]. However, if this condition is not met, initially formed 0°-oriented microstructures are gradually replaced by a dominant 45°-oriented microstructure [46]. Therefore, the rapid solidification characteristics of the L-PBF process difficult to form a 0°-oriented microstructure continuously.

Fig. 5 schematically illustrates the sequence of microstructure formation in the as-built condition determined in this study. Previous studies have shown that the melt-pool shape plays an important role in crystallographic texture formation because it largely determines the local thermal gradient direction, which is generally normal to the melt-pool boundary, and thereby favors cellular growth along the corresponding direction [15,16]. In our previous single-scan study conducted under the same processing conditions, the elongated β cells were observed to be inclined by approximately 45° to the BD, with their elongation direction aligned with the <001> preferential growth direction of the β phase [31]. Under bidirectional scanning along the + x and −x directions, these elongated β cells with <001> orientation are stabilized, resulting in the preferential alignment of the

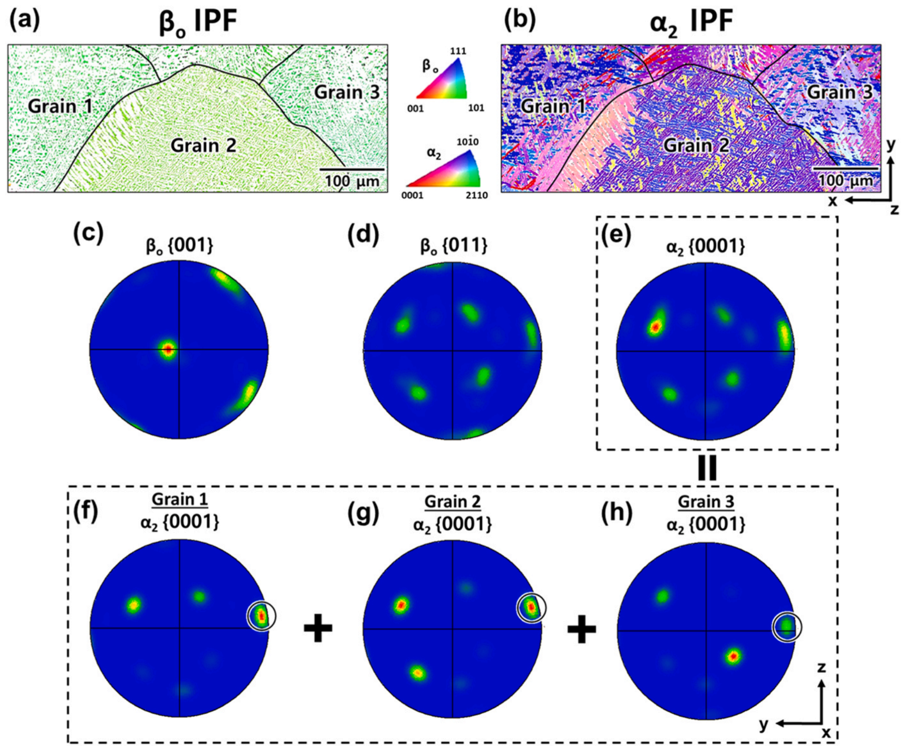

Fig. 4. IPF maps and PFs of the β_o phase and α_2 phases obtained from a large area of the x-y plane. (a,b) IPF maps of the β_o phase and α_2 phases. (c,d) PFs of the β_o phase and (e) PF of the α_2 phase, which follows the Burger OR. The PF of the α_2 phase shown in (e) corresponds to the combined contribution of partial PFs obtained from each β_o grain (grain 1–3), as illustrated in (f–h).

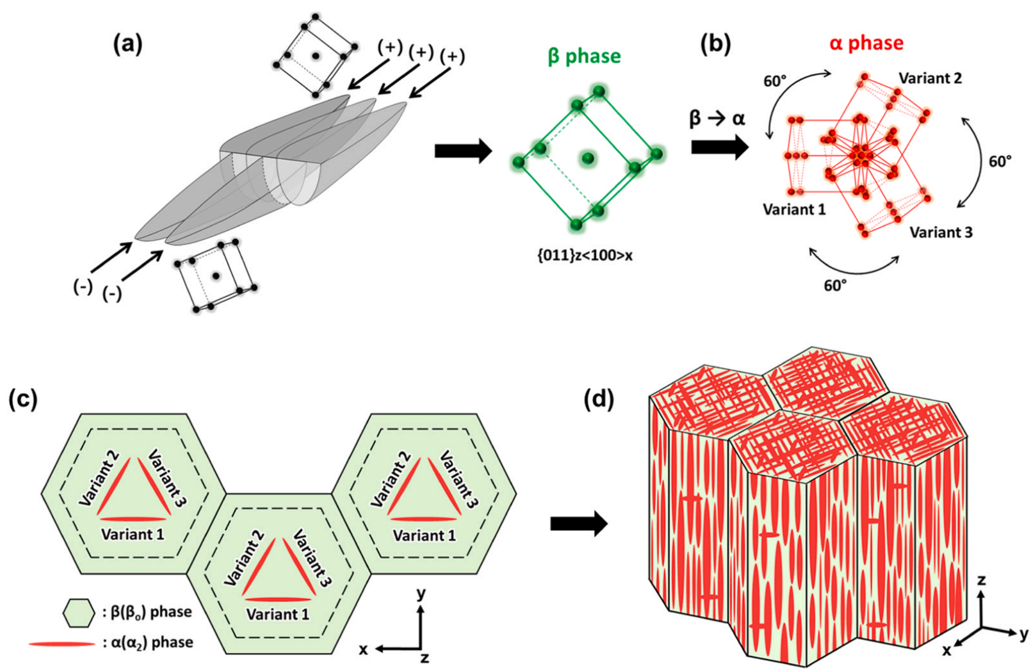

Fig. 5. A schematic representation of the microstructure evolution observed in this study, including the crystallographic texture of the primary β phase, variant selection during the β → α phase transformation, and the final oriented β_o/α_2 microstructure. Please see the text for further details.

<110> direction parallel to the BD (Fig. 5a). Subsequently, the β phase transformed to α phase following Burger OR, allowing twelve possible α variants from six-fold $\{110\}_\beta$ planes. The variant selection is predominantly represented by the clusters consisting of three strongly selected α variants with 60° angles to each other (Fig. 5b), reducing shape strain during the rapid solidification [38]. The formation of three α variants exhibiting 60° angular relationships was repeatedly formed within individual β grains during the early stage of the β → α phase transformation (Fig. 5c). However, the horizontally oriented variant, with its $\{0001\}_{\alpha_2}$ planes is parallel to BD (0°), is gradually suppressed as the L-PBF process progresses. Instead, two predominant types of α variants are induced, with their $\{0001\}_{\alpha_2}$ planes inclined at ± 45° to the BD.

Consequently, these variants were morphologically aligned along the BD as the L-PBF process continued, resulting in the formation of an oriented β_o/α_2 microstructure in the y–z plane (Fig. 5d).

3.2. Microstructural characteristics after heat treatment

Based on the characterized microstructure of the as-built Ti−44Al−6Nb−1.2Cr alloy fabricated by the L-PBF process, no α_2/γ lamellar structure was observed. Therefore, a heat treatment was carried out to promote the formation of lamellae, and the resulting microstructure is shown in Fig. 6. Compared with Fig. 2b, the SEM-BSE image revealed no significant morphological changes after heat treatment, indicating that the overall microstructure remained similar to that of the as-built condition. The oriented β_o/α_2 microstructure was predominantly aligned parallel to the BD, with a minor fraction showing horizontal orientation in the y–z plane (Fig. 6a). In addition, higher-magnification SEM-BSE observation exhibited the formation of lamellae within the α_2 phase, which were inclined at ± 45° and 0° with respect to the BD (Fig. 6b). These lamellar features were also consistently observed in the TEM image (Fig. 6c).

In addition, the crystallographic texture of the β_o and α_2 phases was re-examined using SEM-EBSD after heat treatment. Herein, the γ phase was excluded from the analysis because its fine nano-scale lamellar structure could not be clearly resolved by SEM-EBSD. There were no significant changes in the crystallographic texture after heat treatment. The IPF and PFs of the β_o phase consistently revealed that the $<110>_{\beta o}$ was aligned with the BD (Fig. 7a–c), while the α_2 phase maintained the Burgers OR with the β_o phase (Figs. 7c and 7e–g). Furthermore, the α_2 variants still exhibited three α_2 variant configurations (Fig. 7d–g). Additional observation over a wider region revealed that within the columnar colonies aligned along the BD, two main types of α_2 variants were present whose $\{0001\}_{\alpha 2}$ planes were inclined at ± 45° to the BD. Note that the lamellar orientation was found to be parallel to the $\{0001\}_{\alpha 2}$ planes in each α_2 variant region (Fig. 7h–j). This finding suggests that the β_o texture and the sequential α_2 variant selection in the as-built condition control the lamellar orientation after heat treatment, owing to the Burgers OR and Blackburn OR, respectively.

In order to obtain a more detailed understanding of the lamellar characteristics, TEM observations were additionally conducted (Fig. 8), showing a fine lamellar spacing of approximately 40 nm. Furthermore, the TEM observations interestingly revealed discrepancies in the lamellar microstructure. As shown in Fig. 8a, the low magnification of the TEM image displayed a lamellar morphology resembling the conventional α_2/γ lamellar structure commonly observed in γ-TiAl alloys. However, the corresponding selected area electron diffraction (SAED) patterns showed a distinct difference (Fig. 8b). The incident beam direction was aligned along the $<11\bar{2}0>$ α_2 zone axis, with the lamellar interfaces viewed edge-on. Notably, the sixfold repetition of diffraction spots (indicated by green arrows) was observed along the $[0002]\alpha_2$ axis, suggesting the presence of a long-period stacking ordered (LPSO) structure. Additionally, the [010] zone axis provides the information to determine the R and H structures of the LPSO, e.g., the H structure indicates the angle of 90° between the (100) and (006) [47,48]. The high-magnification TEM images, together with their fast Fourier transformation (FFT) images, clearly confirmed distinct diffraction spots (Fig. 8c–e). Furthermore, the inverse fast Fourier transform (IFFT) images showed different atomic stacking sequences between the α_2 phase and the LPSO structure (Fig. 8f–g). The α_2 phase exhibited a stacking sequence of …ABABABAB…, whereas the LPSO structure displayed a stacking sequence of …ABCBACA…. Thus, these observations confirm the formation of the α_2/6H-LPSO lamellar microstructure rather than the conventional α_2/γ lamellar microstructure typically observed in γ-TiAl alloys.

In general, the phase transformation mechanism of the α_2/γ lamellar microstructure in γ-TiAl alloys involves stacking faults generated by partial dislocations in the α_2 phase. These stacking faults locally modify the original hexagonal close-packed (HCP) stacking sequence and generate a metastable face-centered cubic arrangement, which subsequently undergoes atomic ordering to form the γ phase [49]. However, a recent study proposed an alternative $\alpha_2 \rightarrow \gamma$ lamellar transformation pathway involving an intermediate 6H structure [50]. In this mechanism, alternating positive and negative stacking faults are introduced on layers of the α_2 phase, thereby minimizing the net shear strain and transforming the original HCP stacking sequence into a periodic 6H structure. Therefore, the formation of the 6H-LPSO structure may be closely associated with the generation of periodic stacking faults in the α_2 phase. On this basis, the rapid cooling inherent to L-PBF results in the retention of an Al-supersaturated α_2 phase. Since an increase in Al content has been reported to increase the stacking-fault probability in HCP Ti–Al alloys [51], Al supersaturation may enhance the tendency for stacking-fault formation in the α_2 phase and thereby favor the formation of the 6H-LPSO structure. Furthermore, the 6H-LPSO structure has also been observed in conventionally processed TiAl alloys subjected to rapid cooling, suggesting that a high cooling rate is an important factor in its formation [52,53].

3.3. Tensile properties of heat-treated specimen

The tensile properties of the heat-treated Ti−44Al−6Nb−1.2Cr alloy fabricated via the L-PBF process were evaluated at both room temperature (RT) and 800 °C, with the representative tensile stress–strain curves shown in Fig. 9a. Herein, the tensile specimen and fixture were fastened through frictional force, leaving a small gap between the contacting surfaces. During tensile loading, relative displacement filled the gap, resulting in an apparent anomalous elastic response. However, this behavior was observed only within the elastic deformation region, and

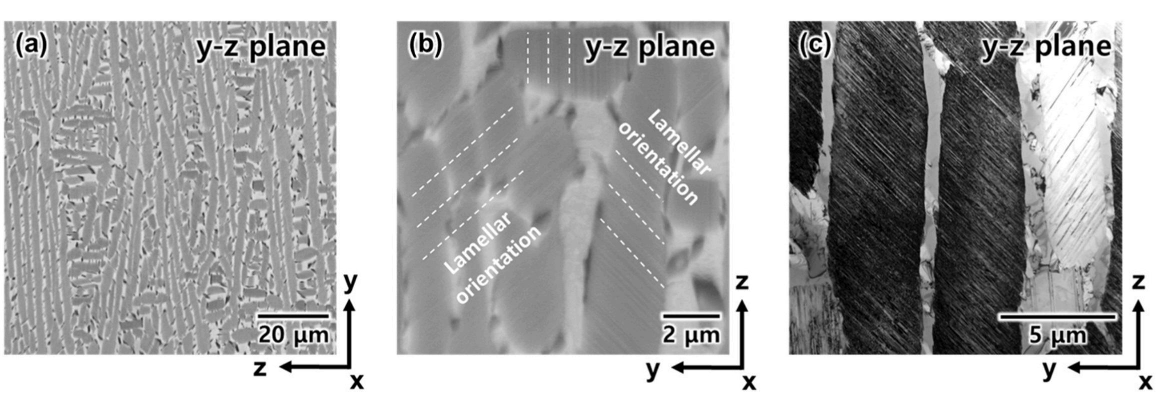

Fig. 6. (a) SEM-BSE image of the heat-treated specimen in the y-z plane. (b) Higher-magnification SEM-BSE image and (c) TEM image confirming the formation of lamellar microstructure.

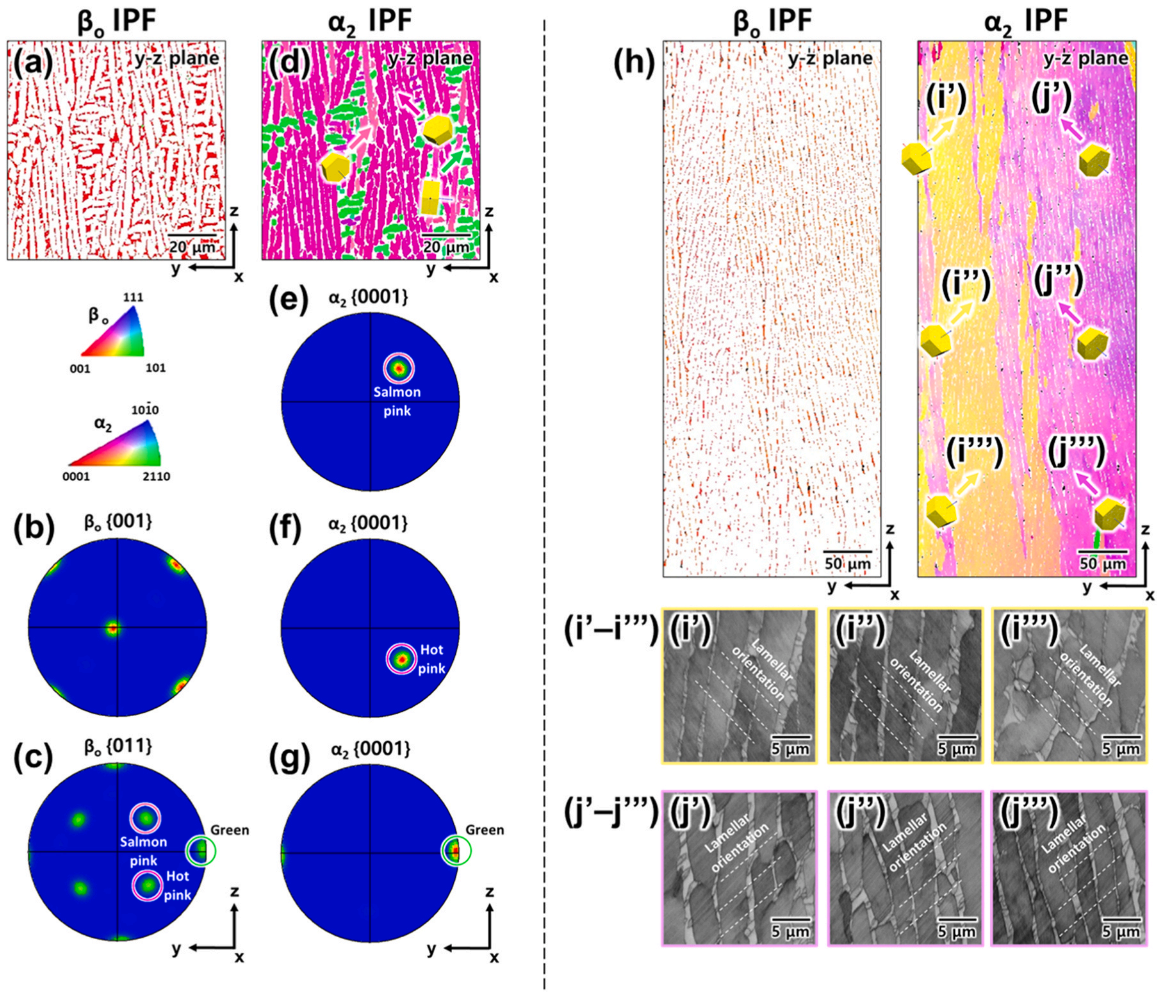

Fig. 7. Crystallographic texture analysis of the heat-treated specimen in the y-z plane: (a) β_o IPF map, (b, c) β_o PFs, (d) α_2 IPF map, (e–g) partial α_2 PFs. (h) shows large-area IPFs for the β_o and α_2 phases. (i′–i‴ and j′–j‴) confirm that the lamellae are oriented along the {0001}α_2 plane of the crystal lattice.

similar phenomena have been reported in a previous study [54]. In addition, the tensile strength to fracture was 475.2 ± 52.1 MPa at RT. A distinct yield behavior was not observed due to the intrinsically brittle nature of the γ-TiAl alloys [54,55]. Therefore, further optimization of the heat-treatment condition is required to improve the ductility at RT, although the evaluated values were comparable to those of other conventionally processed γ-TiAl alloys [56]. On the other hand, the yield strength (YS), ultimate tensile strength (UTS), and elongation (EL) at 800 °C were 523.7 ± 8.5 MPa, 705.5 ± 21.4 MPa, and 8.5 ± 1.4%. For comparison, the microstructure and tensile properties of the as-cast alloy with the same nominal composition are presented in Supplementary Fig. S2. The as-cast specimen exhibited a conventional multiphase microstructure consisting of β_o phase, γ phase, and α_2/γ lamellar colonies. Furthermore, the as-cast alloy exhibited a tensile strength to fracture of 368.5 ± 77.8 MPa at RT, while its YS, UTS, and EL at 800 °C were 363.6 ± 0.1 MPa, 481.2 ± 2.9 MPa, and 2.1 ± 0.1%, respectively.

Notably, as shown in Fig. 9b, the heat-treated Ti−44Al−6Nb−1.2Cr alloy fabricated by the L-PBF process in this study is positioned near the upper limit of reported high-temperature tensile properties among various γ-TiAl alloys produced by different processing methods [9,54,56–71], except for those having highly preferred lamellar orientations in the γ-TiAl matrix along with aligned TiB whiskers produced through hot extrusion [64]. Moreover, compared with the as-cast counterpart having the same nominal composition, the L-PBF-fabricated and heat-treated specimen exhibited significantly higher UTS and EL at 800 °C. These results indicate that the improved high-temperature tensile properties were primarily associated with the microstructural characteristics developed through the L-PBF process and subsequent heat treatment.

The enhancement of YS and UTS can be explained by several microstructural factors. In particular, the refined microstructure induced by the rapid solidification characteristics of the L-PBF process likely contributed to strengthening through the Hall-Petch relationship [72], as also reported in previous studies [12,73]. In general, conventionally cast γ-TiAl alloys exhibit relatively coarse microstructures, consisting of elongated β_o phase, α_2/γ lamellar colonies, and γ phase [35]. Such coarse microstructures provide fewer phase interfaces and grain boundaries that can impede dislocation motion during deformation. In contrast, the refined microstructure formed in the L-PBF specimens introduced a significantly higher density of effective barriers against dislocation movement. As shown in Figs. 10a and 10b, TEM observations of the deformation-induced dislocation structures revealed the formation of dislocation arrays within the γ phase and α_2/6H-LPSO lamellae, suggesting that these regions preferentially accommodated plastic deformation during tensile loading. Pronounced dislocation pile-up was observed particularly at the β_o/γ and β_o/α_2-6H-LPSO interfaces. In general, lamellae inclined at approximately 45° to the loading direction are considered favorable for plastic deformation in γ-TiAl alloys and therefore tend to exhibit relatively low strength [21,22]. However, the β_o phase aligned nearly parallel to the BD acted as barriers to dislocation motion and restricted dislocation transfer across the interfaces. Therefore, dislocations accumulated preferentially at the

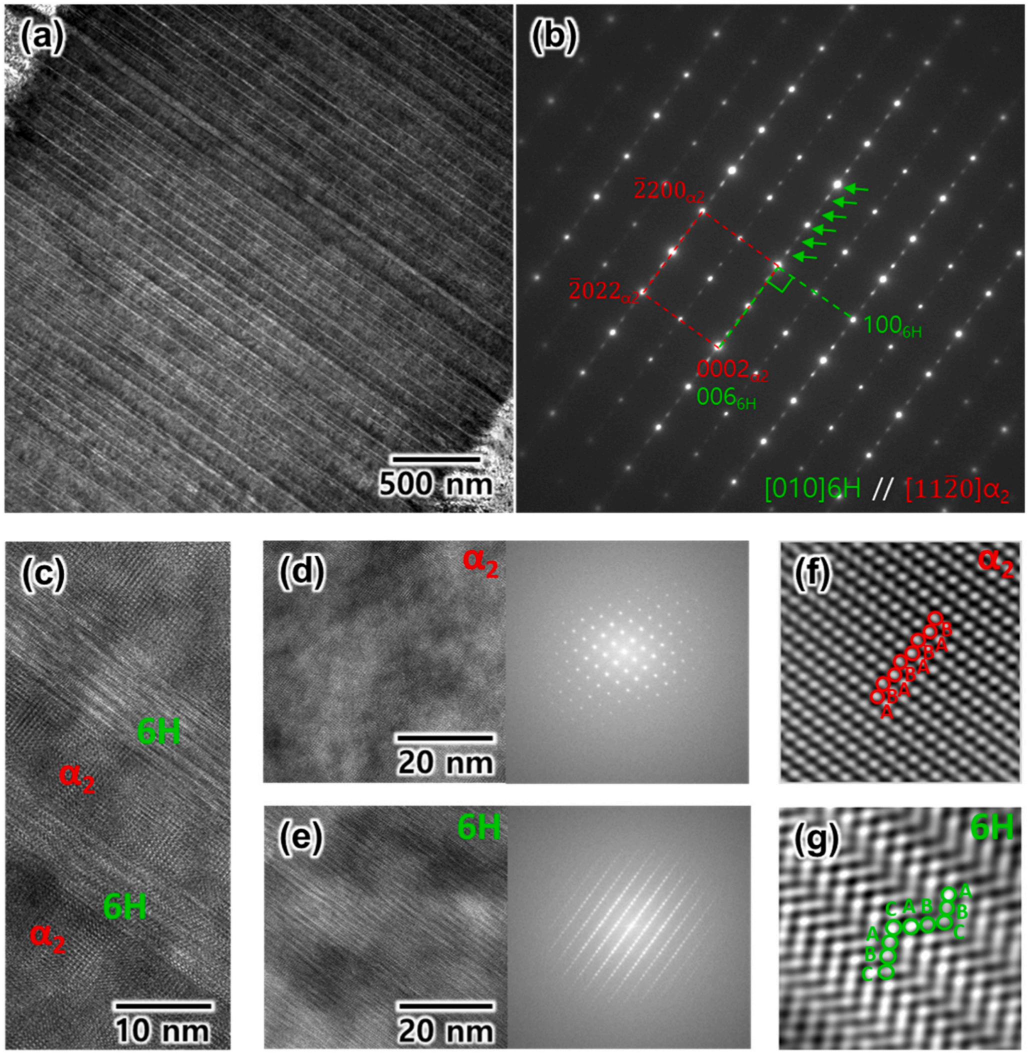

Fig. 8. (a,b) Overview TEM image of the lamellar microstructure with the corresponding SAED pattern, indicating the α_2/6H-LPSO lamellae. (c) Further magnified TEM image in the α_2/6H-LPSO lamellar area, (d,e) images of the α_2 and 6H-LPSO phases with their corresponding FFT patterns, and (f,g) IFFT images illustrating the stacking sequence of the α_2 and 6H-LPSO structure, respectively.

β_o/α_2-6H-LPSO interfaces, contributing to localized stress accumulation and strengthening. In addition, further investigation is required to understand the deformation behavior of the α_2/6H-LPSO lamellae. Nevertheless, dislocation tangles were rarely observed at the α_2/6H-LPSO interfaces, and dislocations tended to move along the lamellar direction, forming dislocation arrays [74]. These observations suggest that the presence of the 6H-LPSO phase may contribute to additional strengthening through strain hardening [75,76]. These aspects are still under investigation and will be described in detail elsewhere.

On the other hand, the EL can be explained in terms of the observed fracture morphology and crack-propagation characteristics. Fig. 11 reveals the fracture surface morphology of the heat-treated Ti−44Al−6Nb−1.2Cr alloy samples after tensile testing. The results indicate that the fracture surface exhibited a distinct step-like morphology irrespective of the testing temperature. The fracture surface was dominated by cleavage planes, which are typically associated with a brittle fracture appearance at RT (Fig. 11a). On the other hand, although the overall fracture surface still retained the step-like characteristics, additional surface features were present at 800°C. The dimples were observed in limited localized areas, and these dimpled regions occasionally appeared (Fig. 11b). In particular, these features were only limited to localized regions, suggesting the occurrence of local plastic deformation at 800 °C without altering the overall fracture behavior. Moreover, tortuous crack propagation accompanied by crack dispersion, deflection, and branching was observed in the side view of the tensile specimen, indicating enhanced damage tolerance (Fig. 11c). In the present microstructure, the β_o/α_2 lamellae were aligned nearly parallel to the loading direction, whereas the inherited α_2/6H-LPSO lamellae were predominantly inclined to the loading direction. The coexistence of these differently oriented lamellae caused propagating cracks to repeatedly interact with lamellar interfaces having different orientations. These interactions hindered stress transfer and altered the crack-propagation direction, thereby reducing the effective crack-driving force. In addition, cracks in γ-TiAl alloys generally propagate along lamellar boundaries [77,78]. The jagged crack path observed in the present study indicates that the differently aligned lamellae acted as effective barriers to crack propagation. These combined crack-propagation behaviors indicate that the highly oriented and inherited α_2/6H-LPSO lamellar microstructure effectively dissipates local stresses, thereby enabling greater plastic accommodation and contributing to the enhanced EL. Consequently, this study highlights the effectiveness of the highly oriented β_o/α_2 and α_2/6H-LPSO lamellar microstructure in achieving an enhanced balance between strength and ductility at high temperature, while offering a new approach for microstructural tailoring of γ-TiAl alloys fabricated via the L-PBF

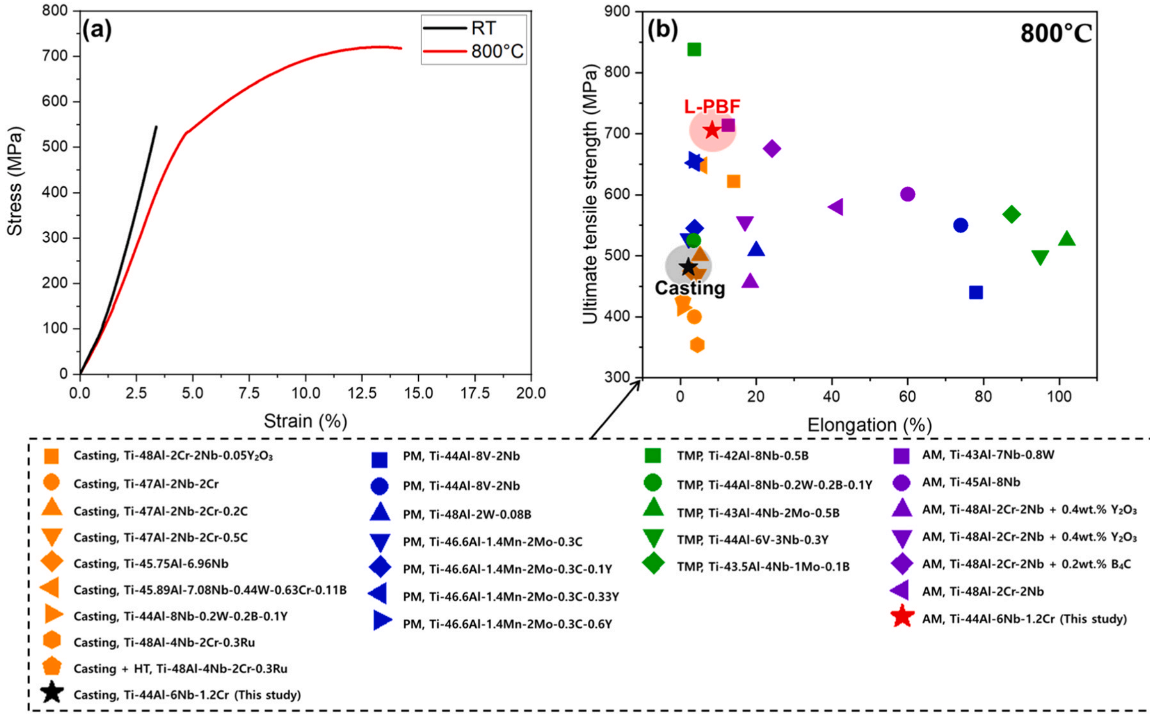

Fig. 9. (a) Representative tensile stress–strain curves of the heat-treated Ti−44Al−6Nb−1.2Cr alloy specimens at RT and 800 °C, and (b) Comparison of the tensile strength and elongation of γ-TiAl alloys at 800 °C fabricated via different manufacturing methods [9,54,56–71].

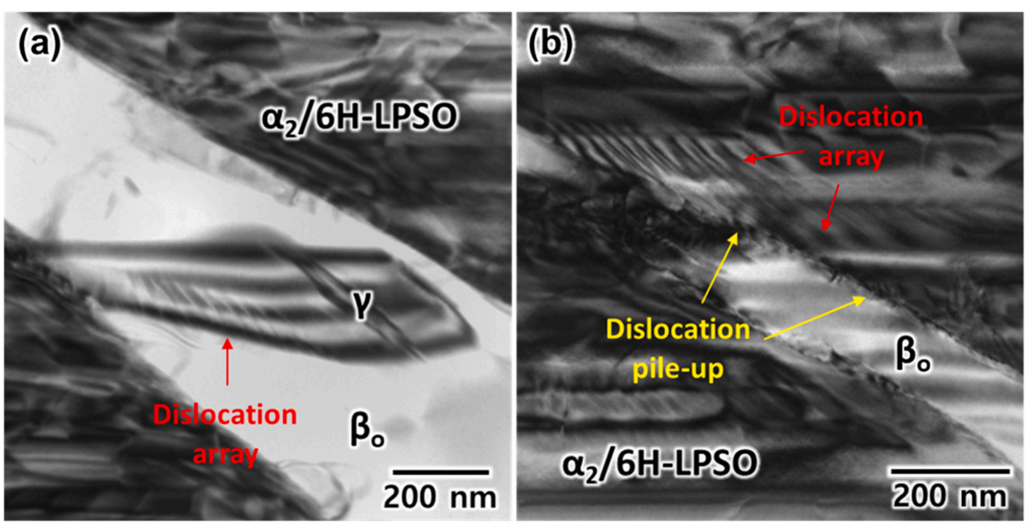

Fig. 10. TEM images of the deformed Ti−44Al−6Nb−1.2Cr alloy. (a) Formation of dislocation arrays within the γ phase and (b) dislocation pile-up observed near the interface between the β_o phase and α_2/6H-LPSO lamellae.

process.

4. Conclusions

In this study, the formation of a highly oriented lamellar microstructure and its effect on the mechanical properties of a β-solidifying γ-TiAl alloy fabricated via L-PBF and subsequent heat treatment were comprehensively investigated. The following main conclusions can be drawn:

1. A dense Ti−44Al−6Nb−1.2Cr alloy was successfully fabricated using optimized L-PBF processing parameters. The strong single-crystalline-like texture formation in the primary β phase and subsequent α variant selection collectively resulted in the formation of predominantly directional β_o/α_2 lamellae.
2. The α_2/6H-LPSO lamellae were aligned parallel to the $(0001)_{\alpha_2}$ plane after heat treatment, indicating that the orientation of the α_2/6H-LPSO structure was strongly governed by the as-built crystallographic texture and α_2 variant selection behavior.
3. The refined microstructure induced by the rapid solidification characteristics of the L-PBF process and the highly oriented lamellar microstructure enhanced the mechanical strength by effectively impeding dislocation motion, while the latter microstructural characteristic promoted crack deflection, branching, and tortuous crack propagation, thereby improving damage tolerance and elongation.

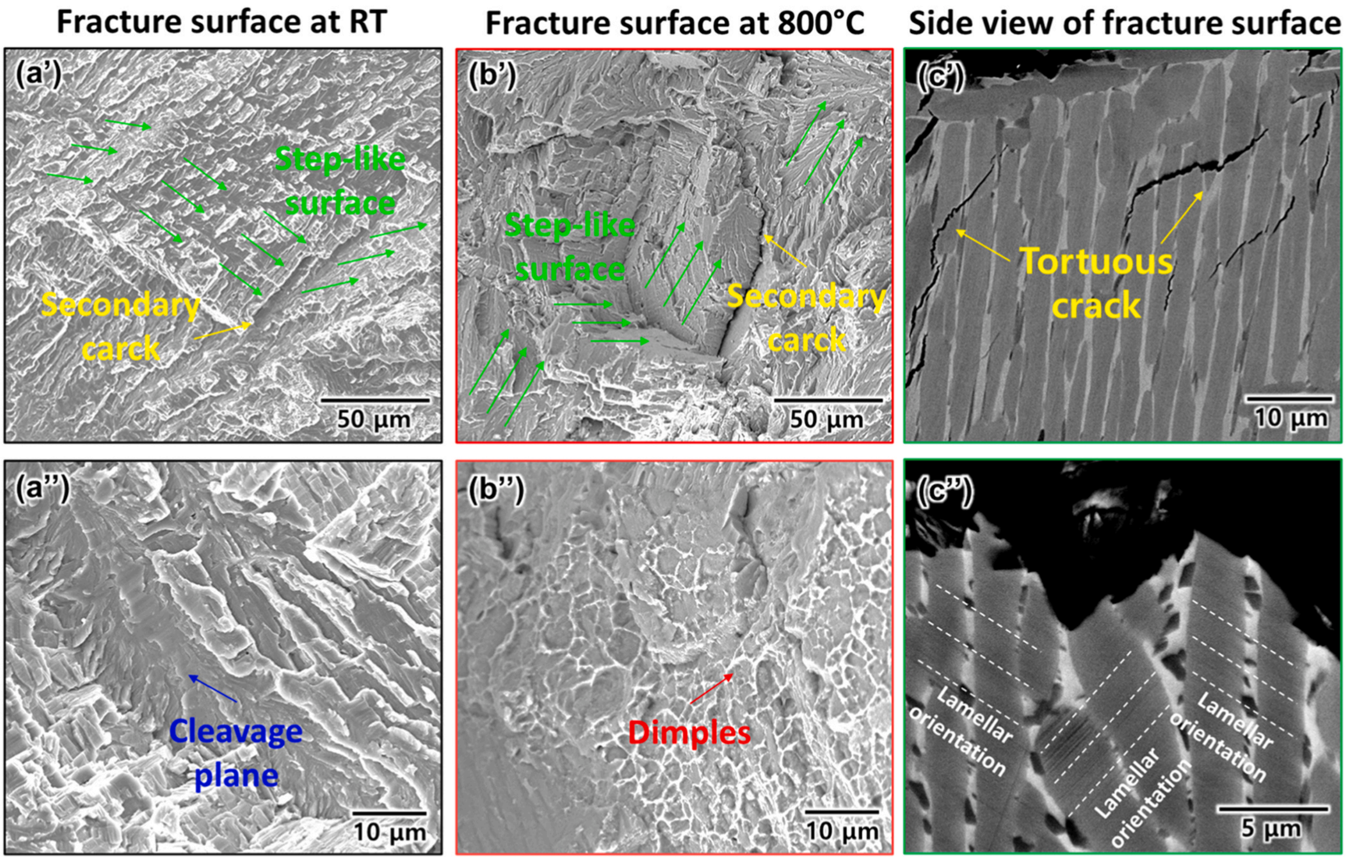

Fig. 11. Fracture surface morphology of the heat-treated Ti−44Al−6Nb−1.2Cr alloy samples. (a, b) Low and high magnification SEM images of the fracture surfaces after tensile testing at RT and 800°C, respectively. (c) Side-view SEM-BSE images near the fracture surface showing crack propagation.

CRediT authorship contribution statement

Takayoshi Nakano: Writing – review & editing, Supervision, Resources, Funding acquisition, Conceptualization. **Sung-Hyun Park:** Writing – original draft, Investigation, Formal analysis, Data curation, Conceptualization. **Ozkan Gokcekaya:** Writing – review & editing, Investigation, Data curation, Conceptualization. **Kazuhisa Sato:** Investigation, Formal analysis, Data curation. **Hyoung Seop Kim:** Writing – review & editing, Supervision. **Myung-Hoon Oh:** Writing – review & editing, Supervision.

Declaration of Competing Interest

The authors declare that they have no known competing financial interests or personal relationships that could have appeared to influence the work reported in this paper.

Acknowledgements

This work was partly supported by CREST-Nanomechanics: Elucidation of Macroscale Mechanical Properties Based on Understanding Nanoscale Dynamics for Innovative Mechanical Materials (Grant No. JPMJCR2194) from the Japan Science and Technology Agency (JST). The authors thank Prof. Dr. Satoshi Ichikawa for his help with TEM observations.

Appendix A. Supporting information

Supplementary data associated with this article can be found in the online version at doi:10.1016/j.jallcom.2026.190423.

Data Availability

Data will be made available on request.

References

[1] Y.-W. Kim, Intermetallic alloys based on gamma titanium aluminide, JOM 41 (1989) 24–30.
[2] M. Yamaguchi, High temperature intermetallics-with particular emphasis on TiAl, Mater. Sci. Technol. 8 (1992) 299–307.
[3] J. Aguilar, A. Schievenbusch, O. Kättlitz, Investment casting technology for production of TiAl low pressure turbine blades – process engineering and parameter analysis, Intermetallics 19 (2011) 757–761.
[4] B.P. Bewlay, S. Nag, A. Suzuki, M.J. Weimer, TiAl alloys in commercial aircraft engines, Mater. High. Temp. 33 (2016) 549–559.
[5] T. Tetsui, Development of a TiAl turbocharger for passenger vehicles, Mater. Sci. Eng. A 329331 (2002) 582–588.
[6] P. Bartolotta, J. Barrett, The use of cast Ti-48AI-2Cr-2Nb in jet engines, JOM 49 (1997) 48–50.
[7] C. Yuan, X. Cheng, G.S. Holt, D. Shevchenko, P.A. Withey, Investment casting of Ti–46Al–8Nb–1B alloy using moulds with CaO-stabilized zirconia face coat at various mould pre-heat temperatures, Ceram. Int. 41 (2015) 4129–4139.
[8] S. Lee, M.-S. Shin, Y.-J. Kim, Development of non-reactive mold for investment casting of Ti-48Al-2Cr-2Nb Alloys, Metall. Mater. Trans. B 51 (2020) 861–869.
[9] M. Todai, T. Nakano, T. Liu, H.Y. Yasuda, K. Hagihara, K. Cho, M. Ueda, M. Takeyama, Effect of building direction on the microstructure and tensile properties of Ti-48Al-2Cr-2Nb alloy additively manufactured by electron beam melting, Addit. Manuf. 13 (2017) 61–70.
[10] K. Cho, H. Kawabata, T. Hayashi, H.Y. Yasuda, H. Nakashima, M. Takeyama, T. Nakano, Peculiar microstructural evolution and tensile properties of β-containing γ-TiAl alloys fabricated by electron beam melting, Addit. Manuf. 46 (2021) 102091.
[11] J. Knörlein, M.M. Franke, M. Schloffer, C. Körner, In-situ aluminum control for titanium aluminide via electron beam powder bed fusion to realize a dual microstructure, Addit. Manuf. 59 (2022).
[12] M.S. Wang, E.W. Liu, Y.L. Du, T.T. Liu, W.H. Liao, Cracking mechanism and a novel strategy to eliminate cracks in TiAl alloy additively manufactured by selective laser melting, Scr. Mater. 204 (2021) 114151.

[13] P. Gao, W. Huang, H. Yang, G. Jing, Q. Liu, G. Wang, Z. Wang, X. Zeng, Cracking behavior and control of β-solidifying Ti-40Al-9V-0.5Y alloy produced by selective laser melting, J. Mater. Sci. Technol. 39 (2020) 144–154.
[14] D. Huang, Y. Zhou, X. Yao, Q. Tan, H. Chang, D. Wang, S. Lu, S. Liu, J. Xu, S. Jin, G. Sha, H. Huang, M. Yan, M.X. Zhang, From crack-prone to crack-free: unravelling the roles of LaB6 in a β-solidifying TiAl alloy fabricated with laser additive manufacturing, Mater. Sci. Eng. A 861 (2022).
[15] T. Ishimoto, K. Hagihara, K. Hisamoto, S.-H. Sun, T. Nakano, Crystallographic texture control of beta-type Ti–15Mo–5Zr–3Al alloy by selective laser melting for the development of novel implants with a biocompatible low Young's modulus, Scr. Mater. 132 (2017) 34–38.
[16] T. Ishimoto, N. Morita, R. Ozasa, A. Matsugaki, O. Gokcekaya, S. Higashino, M. Tane, T. Mayama, K. Cho, H.Y. Yasuda, M. Okugawa, Y. Koizumi, M. Yoshiya, D. Egusa, T. Sasaki, E. Abe, H. Kimizuka, N. Ikeo, T. Nakano, Superimpositional design of crystallographic textures and macroscopic shapes via metal additive manufacturing—Game-change in component design, Acta Mater. 286 (2025).
[17] S.-H. Sun, T. Ishimoto, K. Hagihara, Y. Tsutsumi, T. Hanawa, T. Nakano, Excellent mechanical and corrosion properties of austenitic stainless steel with a unique crystallographic lamellar microstructure via selective laser melting, Scr. Mater. 159 (2019) 89–93, https://doi.org/10.1016/j.scriptamat.2018.09.017.
[18] O. Gokcekaya, T. Ishimoto, S. Hibino, J. Yasutomi, T. Narushima, T. Nakano, Unique crystallographic texture formation in Inconel 718 by laser powder bed fusion and its effect on mechanical anisotropy, Acta Mater. 212 (2021) 116876.
[19] S.H. Park, O. Gokcekaya, T. Nitomakida, T. Nakano, Effects of heat accumulation strategies on defects and microstructure of pure chromium fabricated by laser powder bed fusion: an experimental and numerical study, J. Mater. Res. Technol. 33 (2024) 7333–7344.
[20] S.H. Park, F. Ayten, A.G. Bulutsuz, O. Gokcekaya, M.E. İlgazi, H. Yilmazer, B. Dikici, T. Nakano, Wear and corrosion performance of textured Hastelloy-X fabricated by laser powder bed fusion: process window and microstructural features, J. Mater. Res. Technol. 39 (2025) 6156–6168.
[21] H. Inui, M.H. Oh, A. Nakamura, M. Yamaguchi, Room-temperature tensile deformation of polysynthetically twinned (PST) crystals of TiAl, Acta Metall. Mater. 40 (1992) 3095–3104.
[22] G. Chen, Y. Peng, G. Zheng, Z. Qi, M. Wang, H. Yu, C. Dong, C.T. Liu, Polysynthetic twinned TiAl single crystals for high-temperature applications, Nat. Mater. 15 (2016) 876–881.
[23] H. Jin, Q. Jia, Q. Xian, R. Liu, Y. Cui, D. Xu, R. Yang, Seeded growth of Ti–46Al–8Nb polysynthetically twinned crystals with an ultra-high elongation, J. Mater. Sci. Technol. 54 (2020) 190–195.
[24] Y. Ma, J. Yang, Z. Liu, R. Chen, Deformation behavior of PST-TiAl bicrystals at 800 °C, Mater. Sci. Eng. A 915 (2024).
[25] S. Yokoshima, M. Yamaguchi, Fracture behavior and toughness of PST crystals of TiAl, Acta Mater. 44 (1996) 873–883.
[26] Y. Chen, Y. Cao, Z. Qi, G. Chen, Increasing high-temperature fatigue resistance of polysynthetic twinned TiAl single crystal by plastic strain delocalization, J. Mater. Sci. Technol. 93 (2021) 53–59.
[27] W.G. Burgers, On the process of transition of the cubic-body-centered modification into the hexagonal-close-packed modification of zirconium, Physica 1 (1934) 561–586.
[28] M.J. Blackburn, Some aspects of phase transformation in titanium alloys, in: R. I. Jaffee, N.E. Promisel (Eds.), Sci. Technol. Appl. Titan. Pergamon (1970) 633–643.
[29] S.-H. Park, R. Ozasa, O. Gokcekaya, K. Cho, H.Y. Yasuda, M.-H. Oh, Y.-W. Kim, T. Nakano, Effect of cooling rate on powder characteristics and microstructural evolution of gas atomized β-solidifying γ-TiAl alloy powder, Mater. Trans. 65 (2024) 199–204.
[30] S.H. Park, O. Gokcekaya, R. Ozasa, K. Cho, H.Y. Yasuda, M.H. Oh, T. Nakano, Microstructure evolution of gas-atomized β-solidifying γ-TiAl alloy powder during subsequent heat treatment, Crystals 13 (2023) 1629.
[31] S.H. Park, O. Gokcekaya, R. Ozasa, M.H. Oh, Y.W. Kim, H.S. Kim, T. Nakano, Microstructure and crystallographic texture evolution of β-solidifying γ-TiAl alloy during single- and multi-track exposure via laser powder bed fusion, Met. Mater. Int. 30 (2024) 1227–1241.
[32] S.H. Park, O. Gokcekaya, M.H. Oh, T. Nakano, Effects of hatch spacing on densification, microstructural and mechanical properties of β-solidifying γ-TiAl alloy fabricated by laser powder bed fusion, Mater. Charact. 214 (2024) 114077.
[33] E. Schwaighofer, H. Clemens, S. Mayer, J. Lindemann, J. Klose, W. Smarsly, V. Güther, Microstructural design and mechanical properties of a cast and heat-treated intermetallic multi-phase γ-TiAl based alloy, Intermetallics 44 (2014) 128–140.
[34] J.K. Kim, J.H. Kim, J.Y. Kim, S.H. Park, S.W. Kim, M.H. Oh, S.E. Kim, Producing fine fully lamellar microstructure for cast γ-TiAl without hot working, Intermetallics 120 (2020).
[35] X. Ding, L. Zhang, J. He, F. Zhang, X. Feng, H. Nan, J. Lin, Y.W. Kim, As-cast microstructure characteristics dependent on solidification mode in TiAl-Nb alloys, J. Alloy. Compd. 809 (2019).
[36] M. Wang, Y. Du, H. Wei, W. Liao, From crack-prone to crack-free: eliminating cracks in additively manufactured Ti-48Al-2Cr-2Nb alloy by adjusting phase composition, Mater. Des. 231 (2023).
[37] S.H. Park, O. Gokcekaya, K. Sato, J.S. Park, C.W. Kim, M.H. Oh, S.W. Kim, T. Nakano, Formation of a bi-directional α2/γ lamellar microstructure through crystallographic texture control in a γ-TiAl alloy fabricated by laser powder bed fusion, J. Mater. Res. Technol. 42 (2026) 2625–2637.
[38] S.C. Wang, M. Aindow, M.J. Starink, Effect of self-accommodation on α/α boundary populations in pure titanium, Acta Mater. 51 (2003) 2485–2503.
[39] D. Bhattacharyya, G.B. Viswanathan, R. Denkenberger, D. Furrer, H.L. Fraser, The role of crystallographic and geometrical relationships between α and β phases in an α/β titanium alloy, Acta Mater. 51 (2003) 4679–4691.
[40] N. Gey, M. Humbert, Characterization of the variant selection occurring during the α→β→α phase transformations of a cold rolled titanium sheet, Acta Mater. 50 (2002) 277–287.
[41] P.L. Stephenson, N. Haghdadi, R. DeMott, X.Z. Liao, S.P. Ringer, S. Primig, Effect of scanning strategy on variant selection in additively manufactured Ti-6Al-4V, Addit. Manuf. 36 (2020) 101581.
[42] D. Zhao, J. Fan, Z. Zhang, X. Liang, Z. Chen, Z. Chen, M. Lai, B. Tang, H. Kou, Q. Wang, J. Li, Variant selection mechanism of α phase associated with initial texture and cooling rate in near-α titanium alloy Ti65, Mater. Charact. 223 (2025) 114874.
[43] H. Wang, Q. Chao, L. Yang, M. Cabral, Z.Z. Song, B.Y. Wang, S. Primig, W. Xu, Z. B. Chen, S.P. Ringer, X.Z. Liao, Introducing transformation twins in titanium alloys: an evolution of α-variants during additive manufacturing, Mater. Res. Lett. 9 (2021) 119–126.
[44] Y. Chen, H. Kou, L. Cheng, K. Hua, L. Sun, Y. Lu, E. Bouzy, Crystallography of phase transformation during quenching from β phase field of a V-rich TiAl alloy, J. Mater. Sci. 54 (2019) 1844–1856.
[45] Z. Li, L. Luo, Y. Su, B. Wang, L. Wang, T. Liu, M. Yao, C. Liu, J. Guo, H. Fu, A high-withdrawing-rate method to control the orientation of (γ+α2) lamellar structure in a β-solidifying γ-TiAl-based alloy, Mater. Sci. Eng. A 857 (2022).
[46] I.S. Jung, H.S. Jang, M.H. Oh, J.H. Lee, D.M. Wee, Microstructure control of TiAl alloys containing β stabilizers by directional solidification, 329–331, Mater. Sci. Eng. A (2002) 13–18.
[47] L. Song, X.J. Xu, C. Peng, Y.L. Wang, Y.F. Liang, S.L. Shang, Z.K. Liu, J.P. Lin, Deformation behaviour and 6H-LPSO structure formation at nanoindentation in lamellar high Nb containing TiAl alloy, Philos. Mag. Lett. 95 (2015) 85–91.
[48] Y.M. Zhu, A.J. Morton, J.F. Nie, The 18R and 14H long-period stacking ordered structures in Mg-Y-Zn alloys, Acta Mater. 58 (2010) 2936–2947.
[49] A. Denquin, S. Naka, Phase transformation mechanisms involved in two-phase TiAl-based alloys—I. Lambellar structure formation, Acta Mater. 44 (1996) 343–352.
[50] X. Zhang, C. Li, M. Wu, Z. Ye, Q. Wang, J. Gu, Atypical pathways for lamellar and twinning transformations in rapidly solidified TiAl alloy, Acta Mater. 227 (2022).
[51] E.A. Metzbower, Stacking fault probability determinations in HCP Ti-Al Alloys, Metall. Mater. Trans. B 2 (1971) 3099–3103.
[52] L. Su, Y. Wang, Q. Hu, J. He, Y. Luo, B. Liu, Y. Liu, Metastable phase transformations and mechanical properties of an as-extruded TiAl-based alloy during two-step heat treatment, J. Alloy. Compd. 1005 (2024).
[53] Y. Yu, H. Kou, W. Yi Wang, Y. Wang, F. Qiang, C. Zou, J. Li, Formation of lamellar microstructure in Ti-48Al-7Nb-2.5V-1Cr alloy, Mater. Des. 224 (2022).
[54] H. Zhang, D. Lu, Y. Pei, T. Chen, T. Zou, T. Wang, X. Wang, Y. Liu, Q. Wang, Tensile behavior, microstructural evolution, and deformation mechanisms of a high Nb-TiAl alloy additively manufactured by electron beam melting, Mater. Des. 225 (2023).
[55] D. Huang, Q. Tan, Y. Zhou, Y. Yin, F. Wang, T. Wu, X. Yang, Z. Fan, Y. Liu, J. Zhang, H. Huang, M. Yan, M.X. Zhang, The significant impact of grain refiner on γ-TiAl intermetallic fabricated by laser-based additive manufacturing, Addit. Manuf. 46.
[56] R. Hu, Y. Wu, J. Yang, Z. Gao, J. Li, Phase transformation pathway and microstructural refinement by feathery transformation of Ru-containing γ-TiAl alloy, J. Mater. Res. Technol. 18 (2022) 5290–5300.
[57] Y. Guo, S. Xiao, Y. Chen, J. Tian, Z. Zheng, L. Xu, High temperature tensile properties and fracture behavior of Y2O3-bearing Ti-48Al-2Cr-2Nb alloy, Intermetallics 126 (2020).
[58] Q. Wang, H. Ding, H. Zhang, R. Chen, J. Guo, H. Fu, Variations of microstructure and tensile property of γ-TiAl alloys with 0–0.5 at% C additives, Mater. Sci. Eng. A 700 (2017) 198–208.
[59] X. Xu, H. Ding, H. Huang, H. Liang, R. Chen, J. Guo, H. Fu, Microstructure and elevated temperature tensile property of Ti–46Al–7Nb-(W,Cr,B) alloy compared with binary and ternary TiAl alloy, Mater. Sci. Eng. A 807 (2021).
[60] S. Zhang, N. Tian, D. Li, J. Li, F. Jin, G. Wang, S. Tian, Microstructure evolution and fracture mechanism of a TiAl–Nb alloy during high-temperature tensile testing, Mater. Sci. Eng. A 831 (2022).
[61] M. Wang, R. Guo, H. Niu, H. Zhang, W. Yang, Phase transformations and mechanical behavior of β-type TiAl intermetallics fabricated via hot isostatic pressing of pre-alloyed powder, Mater. Sci. Eng. A 966 (2026).
[62] T. Voisin, J.P. Monchoux, M. Thomas, C. Deshayes, A. Couret, Mechanical properties of the TiAl IRIS Alloy, Metall. Mater. Trans. A Phys. Metall. Mater. Sci. 47 (2016) 6097–6108.
[63] Y. Wu, S.K. Hwang, Microstructural refinement and improvement of mechanical properties and oxidation resistance in EPM TiAl-based intermetallics with yttrium addition, Acta Mater. 50 (2002) 1479–1493.
[64] G. Yang, R. Li, J. Park, X.X. Yang, L. Cheng, W. Song, X. Zhao, S.W. Kim, Synergistic enhancement of strength and ductility in TiB whisker-reinforced high Nb containing TiAl alloys via hot extrusion and subsequent heat treatment, Mater. Sci. Eng. A 945 (2025).
[65] S. Zhang, N. Tian, J. Li, G. Yang, W. Yang, G. Wang, Z. Liu, Y. Li, Microstructure evolution of a forged TiAl-Nb alloy during high-temperature tensile testing, Mater. Charact. 205 (2023).
[66] H.Z. Niu, Y.Y. Chen, S.L. Xiao, L.J. Xu, Microstructure evolution and mechanical properties of a novel beta γ-TiAl alloy, Intermetallics 31 (2012) 225–231.

[67] H.Z. Niu, F.T. Kong, Y.Y. Chen, F. Yang, Microstructure characterization and tensile properties of β phase containing TiAl pancake, J. Alloy. Compd. 509 (2011) 10179–10184.
[68] M. Burtscher, T. Klein, J. Lindemann, O. Lehmann, H. Fellmann, V. Güther, H. Clemens, S. Mayer, An advanced tial alloy for high-performance racing applications, Materials 13 (2020) 1–14.
[69] L. Cai, K. Huang, S. Liu, Z. Jiao, Q. Wang, I. Baker, H. Wu, High-temperature deformation mechanisms in a high-Nb TiAl alloy fabricated by laser metal deposition, Mater. Sci. Eng. A 953 (2026).
[70] B. Gao, H. Peng, H. Yue, H. Guo, C. Wang, B. Chen, Electron beam powder bed fusion of Y2O3/γ-TiAl nanocomposite with balanced strength and toughness, Addit. Manuf. 72 (2023).
[71] H. Yue, H. Gao, C. Zhang, Y. Wang, R. Li, Enhanced strength and ductility of (Ti2AlC and TiB2) -reinforced TiAl alloy fabricated by directed energy deposition, J. Alloy. Compd. 1037 (2025).
[72] N. Hansen, Hall-petch relation and boundary strengthening, Scr. Mater. 51 (2004) 801–806.
[73] K. Mizuta, Y. Hijikata, T. Fujii, K. Gokan, K. Kakehi, Characterization of Ti-48Al-2Cr-2Nb built by selective laser melting, Scr. Mater. 203 (2021).
[74] T. Cao, C. Chen, R. Zhao, X. Lu, G. Zhen, C. Lu, S. Xu, S. Shuai, T. Hu, J. Wang, Z. Ren, Hierarchically heterogeneous microstructure and mechanical properties in laser-directed energy deposition of γ-TiAl alloy through intrinsic cyclic heat treatment, Mater. Sci. Eng. A 910 (2024), https://doi.org/10.1016/j.msea.2024.146867.
[75] G. Zheng, B. Tang, W. Chen, S. Zhao, Y. Xie, X. Chen, J. Li, L. Zhu, Long-period stacking ordering induced ductility of nanolamellar TiAl alloy at elevated temperature, Mater. Res. Lett. 11 (2023) 414–421.
[76] G. Zheng, B. Tang, S. Zhao, Y. Xie, W.Y. Wang, J. Li, L. Zhu, Novel deformation mechanism of nanolamellar microstructure and its effect on mechanical properties of TiAl intermetallics, Mater. Sci. Eng. A 879 (2023).
[77] Y.H. Lu, Y.G. Zhang, L.J. Qiao, Y.-B. Wang, C.Q. Chen, W.Y. Chu, In-situ TEM study of fracture mechanisms of polysynthetically twinned (PST) crystals of TiAl alloys, Mater. Sci. Eng. A 289 (2000) 91–98.
[78] Y. Wang, H. Yuan, H. Ding, R. Chen, J. Guo, H. Fu, W. Li, Effects of lamellar orientation on the fracture toughness of TiAl PST crystals, Mater. Sci. Eng. A 752 (2019) 199–205.